*Article*

# Methacrylated Silk Fibroin Additive Manufacturing of Shape Memory Constructs with Possible Application in Bone Regeneration

**Alessio Bucciarelli[1*], Mauro Petretta[1,2], Brunella Grigolo[1], Laura Gambari[1], Alessandra Maria Bossi[3], Francesco Grassi[1] and Devid Maniglio[4*]**

[1] Laboratorio RAMSES, IRCCS Istituto Ortopedico Rizzoli, Via Giulio Cesare Pupilli, 1, 40136 Bologna, Italy
[2] RegenHU SA, Z.I. du Vivier 22, 1690, Villaz-St-Pierre, Switzerland
[3] Department of Biotechnology, University of Verona, Strada Le Grazie 15, Verona 37134, Italy
[4] Department of Industrial Engineering, BIOtech Research Center, University of Trento, Via delle Regole 101, Mattarello, Trento 38123, Italy
* Correspondence: Alessio.Bucciarelli@ior.it, Devid.Maniglio@unitn.it

**Abstract:**

Methacrylated silk (Sil-MA) is a chemically modified silk fibroin specifically designed to be crosslinkable under UV light. This allows the structuring of this material throught additive manufacturing techniques and then to easily prototype patient specific construct. In this study we used Sil-MA to produce single layer crosslinked structures that can be withdrawal and ejected recovering their shape after rehydration. A complete chemical and physical characterization of the material has been conducted. Additionally, we tested the material biocompatibility according to the International Standard Organization protocols (ISO 10993) ensuring the possibility to use it in future trials. The material was also tested to verify its ability to support the osteogenesis. Two different additive manufacturing techniques have been tested (a Digital Light Processing (DLP) UV projector and a pneumatic extrusion technique) to develop Sil-MA grid. Finally, we provide a proof-of-concept that the printed Sil-MA structures are injectable.

**Keywords:** Silk Fibroin; Sil-MA; 3D Printing; Additive Manufacturing; Tissue Engineering; Bioprinting; Bone Tissue Engineering

## 1. Introduction

Hydrogels are three dimensional (3D) polymeric continuous networks able to entrap a large amount of water. They do not dissolve in water and they maintain they shape due to chemical or physical crosslinking or the entanglement of their polymer chains[1–4]. This abundant amount of water (that can reach 99% of the total weight) makes the use of hydrogel particularly friendly to the biological environment as the human body. Due to their ability to entrap molecules, cells and other factors, and, their facile and versatile fabrication, hydrogels found one of their core applications in the clinical practice (mainly as injectable fillers and wound dressing)[5,6] and in tissue engineering (TE)[6,7].

In TE hydrogels are mainly used with the aim of simulating the extracellular matrix (ECM) and to regenerate damaged biological tissues. This may include the delivery of drugs, cells and factors entrapped into the gel[6,7].In the particular case of Bone Tissue Engineering (BTE) hydrogels have several advantages, their mechanical properties and degradation can be tuned accordingly with the crosslinking degree, they can provide nutrient due to their ability to swell incorporating liquids from outside, and they provide an environments suitable for endogenous cell growth. Moreover, hydrogels are absorbable and they have an excellent integration with surrounding biological tissues limiting the possibility of inflammatory or immune responses[8].

 doi:10.20944/preprints202211.0366.v1



Hydrogels can be formed by both synthetic and natural derived polymers. The last have the advantage to be more similar to the natural tissue and biocompatible, biodegradable, and with a low or no cytotoxicity. Among the various biopolymers available (i.e. Chitosan[9], Keratin[10], Alginate[11], Agarose[12]) Silk Fibroin (SF) is particularly interesting because of its high mechanical strength which makes it a good candidate in the case of structural requirements.

SF is the internal protein of silk fiber and is extracted from it in form of an aqueous solution (regenerated Silk Fibroin, rSF) by chemical processing[13,14]. SF have an excellent mechanical strength[15], is biocompatible[16,17], bioresorbable[18,19], and in forms of gels and films it is transparent[20–22]. Starting form rSF different procedures have been used to develop hydrogels both by physical and chemical crosslinking.

Physical crosslinking is obtained by a change in the protein secondary structure (from random to β-sheet) and is less stable than chemical cross-linking in which the stability is ensured by the formation of a three-dimensional (3D) continuous network by covalent bonding[23]. Chemical crosslinking can be obtained by two approaches. The first consists in promoting the formation of dityrosine and trityrosine crosslinking by the use of different agents with or without an external stimuli (ruthenium and ammonium persulphate and UV irradiation[24], riboflavin and UVA irradiation[25], hydrogen peroxide and horseradish peroxidase[26], Genipin in presence of humidity[27,28]). The latter is a modification of the protein to allow a crosslinking reaction triggered by an on/off UV exposure (photocrosslinking).

Sil-MA (methacrylated silk) is a chemically modified silk fibroin initially designed as bioink to be used in Digital Light Processing (DLP) and Stereolithography (SLA) 3D printing[29,30]. The ability to photocrosslinking is achieved by modifying the lysine side groups of the protein adding a methacrylic functionality that with the addition of a photoinitiator and UV-exposure generates stable chemical crosslinking bonds. The advantage respect previously developed silk photocrosslinking[31–33] is that the entire process is conducted in water making it of great attraction for Tissue Engineering (TE) applications. The produced material is a hydrogel that can be shaped accordingly to the necessities by generating a file containing the design and using light-based 3D printer to produce the final object. This makes the overall technique able to develop patient specific devices as widely discussed in literature[34,35].

Since its development in 2018 Sil-MA has been widely studied as base material for developing different architectures, including but not limited to bone and cartilage scaffolds[34–38], nanoparticles for molecular recognition[39], sealant for clinical applications[40]. The use of Sil-MA as injectable hydrogel has been only recently introduced in case of spinal cord injury[41]. The proposed strategy is the crosslinking after injection, to form the gel *in-situ* allowing the its stabilization in the injection site[40,41]. This has the disadvantage that the possibility to develop complex structures such as the one obtained by 3D printing is lost and the hydrogel is formed as a bulk.

In this work using a previously developed Sil-MA protocol we adopted two 3D printing methodology, a DLP projection and a pneumatic extrusion technique in combination with a Poloxamer support bath to print single layer Sil-MA injectable 3D structures with a possible application in BTE. Sil-MA was produced starting from the raw cocoons and characterized by Fourier Transform Infrared Spectroscopy (FTIR), UV-Vis spectroscopy and Nuclear Magnetic Resonance (NMR) to confirm the presence of the methacrylic groups and quantify them. The rheology of Sil-MA gels and their swelling in water was quantified for different crosslinking time. An initial in-vitro biological evaluation was conducted on the material verifying the biocompatibility of the material in accordance with the International Standard Organization standards (ISO 10993). An additional experiment was conducted using human adipose derived stem cells to prove if Sil-MA can support the osteogenesis. Finally, a withdrawal and release of a s proof-of-concept tructure from a pipette was done demonstrating the ability of shape recovery after the ejection and the re-hydration.

 doi:10.20944/preprints202211.0366.v1



## 2. Results and Discussion

### *2.1. Structural Characterization*

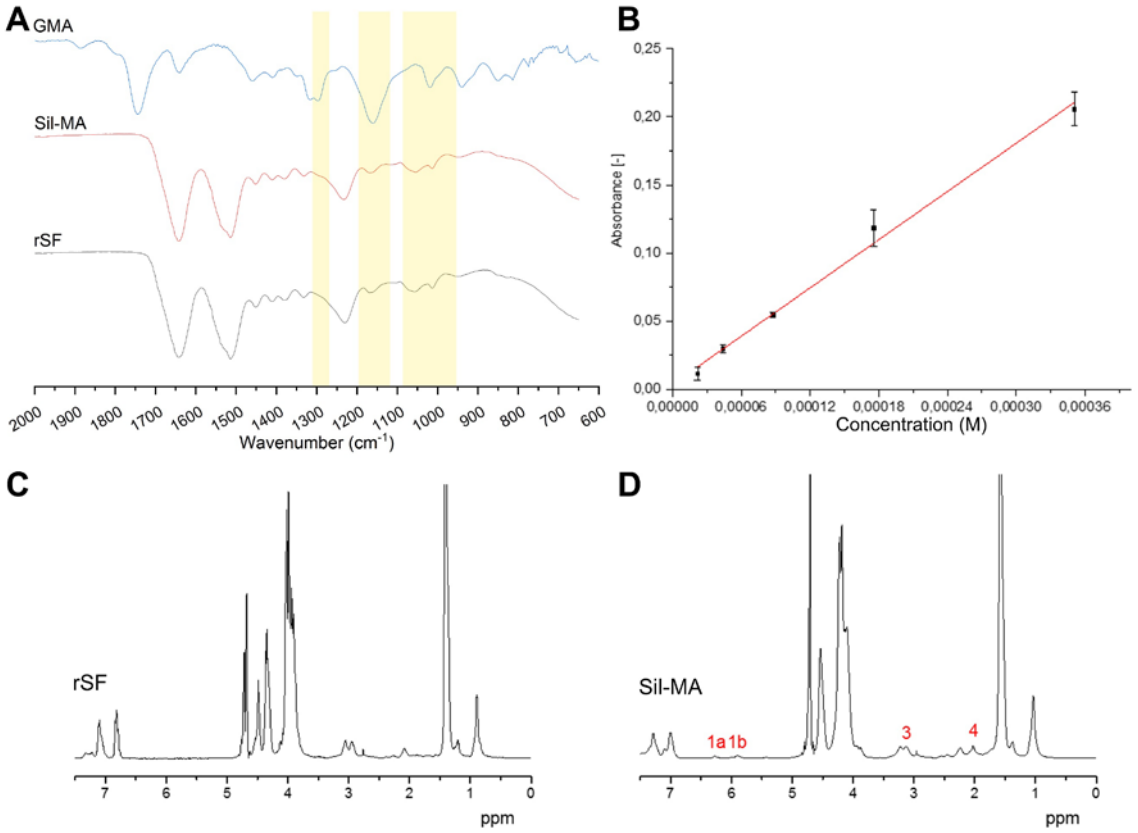


**Figure 1.** (**A**) FTIR spectra of lyophilized sponges of regenerated silk fibroin (rSF) and methacrylated silk fibroin (Sil-MA) as reference the spectra of Glycidyl Methacrylate (GMA) was reported. Several modifications of the Sil-MA spectra compared to the rSF one could be attributed to the presence of functional groups. The yellow areas indicate the modifications. (**B**) Optical calibration to determine the percentage of functional groups in Sil-MA. The calibration was done using β alanine and the TNBS assay. NMR spectra of (**C**) rSF and (**D**) Sil-MA, in red the peaks present in Sil-MA but not in rSF that confirms the functionalization excluding peak 3 which is the lysine contribution.

The presence of functional groups and the protein secondary structure was qualitatively evaluated by infrared spectroscopy (FTIR−ATR). In **Figure 1A**, the comparison between modified (Sil-MA) and regenerated fibroin (rSF) silk fibroin lyophilized sponges is shown. In addition, the spectra collected by a glycidyl methacrylate (GMA) solution is reported as reference. Small variations in the spectra can be attributed to the presence of the functional groups, in accordance with previously published works[29,36]. The presence of the functional group was indicated by the modification of the Sil-MA spectrum compared to the rSF spectrum and traceable to peaks present in the GMA spectrum. In particular modifications were present at 1265 $cm^{-1}$ (CHOH stretching), 1165 $cm^{-1}$ ($CH_2$ wagging stretching) and between 1100 $cm^{-1}$ and 950 $cm^{-1}$ (CH bending of out of plane vinyl groups). Using the calibration curve of **Figure 1B** and the linear regression (**Equation 1**) the calculated percentage of substitution for the produced Sil-MA was DS (%) = 33.1%. A similar result was obtained by the NMR analysis comparing the Sil-MA and the rSF spectra. SF spectrum shows many overlapped signals that can be attributed to the protons of the amino acids of which the protein is composed (alanine, glycine, serine and other minor contributions). Comparing rSF (**Figure 1C**) and Sil-MA (**Figure 1D**) spectra all $CH_3$ and $CH_2$ signals were shifted, while the signals from protons produced by aromatic amino

 doi:10.20944/preprints202211.0366.v1



acids remained unchanged. The reason for this is difficult to understand. Maybe it was due to a different LiBr/$D_2O$ ratio or a different chain folding induced by methacrylation. In Sil-MA spectrum the weak signals of methacrylate groups could be discerned. The methacrylate vinyl group (**1a** and **1b** in **Figure 1D**) and the methyl group (**4, Figure 1D**). The signal indicated with **3** in **Figure 1D** is the lysine signal. This signal was integrated after normalization with respect to the signal at 1 ppm to calculate the degree of GMA substitution, which resulted of DS (%) = 33% in accordance with the TNBS assay and previously published results [29,36].

$$A = 589.225C + 0.004 \quad (1)$$

*2.3 Physicochemical characterization*

The measurements of rheological properties allowed to understand the changes in mechanical properties at different times of exposure to UV light. Three curing times were analyzed: 5 s, 30 s, 1 min. Each sample was analyzed right after photocuring, without adding water, in order to make comparable measurements. Firstly, amplitude sweep test was performed to define the linear viscoelastic region (LVR). Indeed, the rheological properties of a viscoelastic material are independent until a certain value of strain. Beyond this critical strain, the material's behavior is non-linear and the storage modulus declines. The strain sweep test is showed in **Figure 2A**, where storage modulus (G') and the loss modulus (G'') are plotted as function of strain rate. G' and G'' represent the elastic and the viscous part of the hydrogels, respectively. All the crosslinked hydrogels showed nearly constant value of G' and G'' for a wide range of shear strain. Up to 1% shear strain (black line, **Figure 2A**), all the samples seem to be in the linear viscoelastic region. This suggests that the samples structures were undisturbed in all cases. For this reason, 1% shear strain was fixed for the successive frequency sweep test. Interestingly tan δ curves (**Figure 2B**) show a different behavior for the 0.5 s, compared with the other two crosslinking times (30s and 60 sec). While the first, after an initial plateau tend to increase, the latter, after an initial increase show a slight decrease. This can be attributed to the low crosslinking time of the first sample that did not allow a complete crosslinking.

The structure of hydrogels was further characterized with a frequency sweep test (**Figure 2C**), where frequency was varied between 0.1 rad/s and 25 rad/s, while shear rate was kept constant. All the specimens displayed a behavior nearly independent from the frequency, as it is expected from a solid-like material. Indeed, G' showed much larger dependency, exhibiting a more fluid-like is the material. In all samples G' was larger than G'' by a factor of about 40, which indicates that all the hydrogels had an elastic behavior even with low time of UV exposure. We were not able to detect any noticeable difference between 30s and 60s of crosslinking, probably because 30s were sufficient to completely crosslink the gel. For this reason, the swelling test was conducted only on 5s or 30s crosslinked samples. All the tan δ curves reported in **Figure 2D** showed the same trend, as expected the curves were shifted to higher values accordingly with the increasing in the exposure time. This indicates a progressively higher dissipative material.

The result of the swelling test is shown in **Figure 2E**: the weight of samples increased with increasing the hydration time (up to 72 h after crosslinking). Nevertheless, the behavior of the two samples was different. The sample cured for 5 s reached a swelling ratio of about 90%, while the sample cured for 30 s limited the swelling to about 45%, also showing a lower swelling rate. As expected, the reduction of the crosslinking degree, determined by the limited curing time, increased the ability of the gel to adsorb water, permitting a more pronounced expansion of the polymeric network.

Preprints (www.preprints.org) | NOT PEER-REVIEWED | Posted: 21 November 2022 doi:10.20944/preprints202211.0366.v1



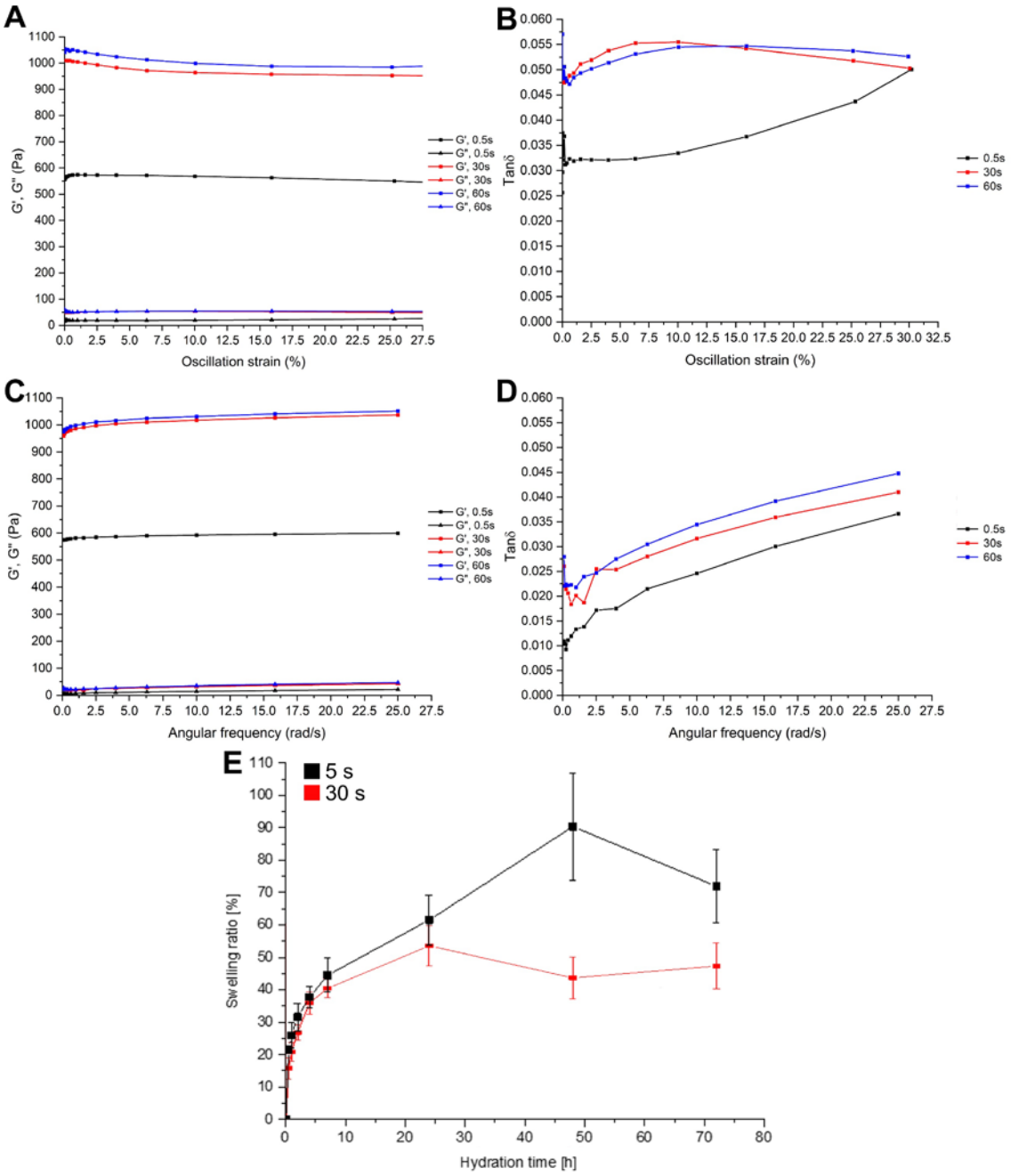


**Figure 2.** (**A**) Storage (G′) and Loss (G′′) modulus reported in function of the oscillation strain (in log scale), all the curves resulted to be linear up to 1%. (**B**) tan δ in function of the oscillation strain, the trend for the 5s crosslinked material was different from the other due to the uncomplete cross-linking. (**C**) G′ and G′′ in function of the angular frequency at constant stain of 1%. (**D**) tan δ in function of the angular frequency with constant strain of 1%.

*2.4 Biological evaluation*

Cytotoxicity assay was performed on Sil-MA to evaluate any possible cytotoxic effect due to the material. This assay is based on the lactate dehydrogenase (LDH) release from damaged cells. Silk fibroin films were used as controls. In **Figure 3A** the result after 48 h of incubation in the conditionated medium is reported. Sil-MA had a low LDH release, almost comparable with rSF and the negative control (Ctrl-) represented by cells grown in normal culture medium. The positive control (Ctrl+) is represented by fully lysate cells (maximum LDH release). According to these results Sil-MA resulted not cytotoxic.

Preprints (www.preprints.org) | NOT PEER-REVIEWED | Posted: 21 November 2022 doi:10.20944/preprints202211.0366.v1



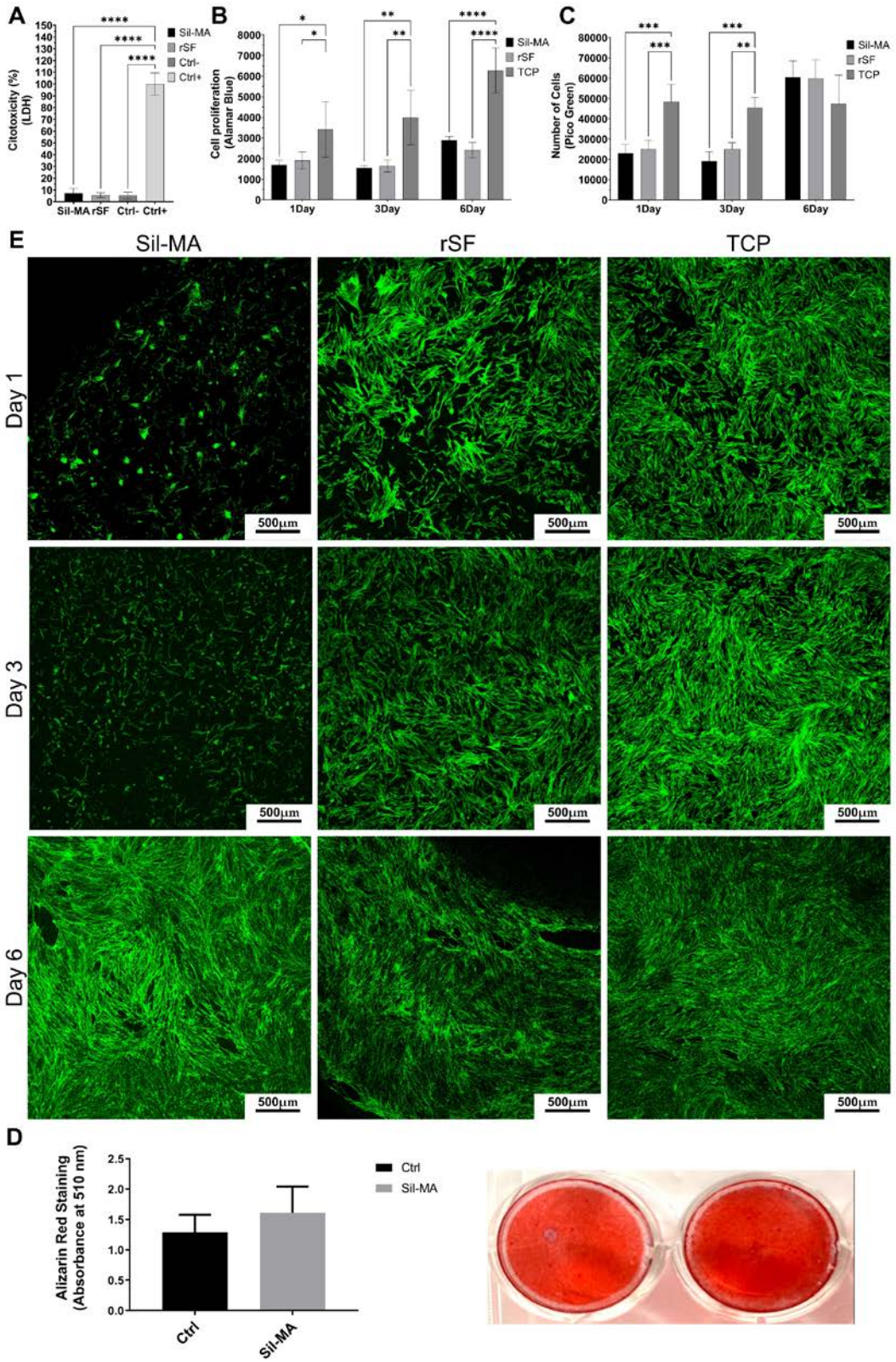


**Figure 3.** (**A**) LDH assay, (**B**) Alamar Blue assay and (**C**) Pico Green assay. (**E**) Confocal images taken at day 1, 3 and 6. (**D**) Alizarin Red Staning

Alamar Blue assay let the evaluation of cell metabolic activity at day 1, 3 and 6. The results are shown in **Figure 3B**. The metabolic activity of Sil-MA films is similar to that of rSF films. The increase of metabolic activity is not so evident from day 1 to day 3, while it

 doi:10.20944/preprints202211.0366.v1



is clearly increasing at day 6. The quite large standard deviations are due to wide variations of biological samples. At each time point, the TCP values are higher than Sil-MA and rSF ones, as expected

**Figure 3C** shows the result of Pico Green assay. The test allows to consider cell proliferation estimating the number of cells at each time point. The number of cells of Sil-MA is similar to that of rSF at each time point; cell proliferation is not so fast at the beginning but increases a lot at day 6. The values seem to be constant at day 1 and day 3, indicating a slowing down in proliferation, that is supported by Alamar Blue results. The number of cells values are reported in detail in **Table 1**. At day 1 and day 3, both Sil-MA and rSF show approximatively the same cell number, while at day 6 it is triplicated. The number of cells on TCP is quite constant during the test, because cells reached confluence at day 1.

In **Figure 3D** the results of Confocal analysis on Sil-MA, rSF and TCP (control, cell cultured on plastic plate) at day 1, 3 and 6 are displayed. The cytoskeleton is stained with Phalloidin i-Fluor 488 and nuclei with DAPI. Silk fibroin materials absorb DAPI, leading to difficulty in identifying the nuclei. For this reason, only cytoskeleton images are reported. Sil-MA samples show low cell adhesion at day 1 and day 3, if compared to rSF and TCP. However, at day 6 good cell adhesion on Sil-MA films is showed; cells show a stretched shape and are well distributed on the film. The adhesion is a bit slow at the beginning, but at day 6 Sil-MA images are comparable to TCP ones. Confocal images are consistent with Alamar Blue and Pico Green assays results.

To assess whether Sil-MA films can support osteogenesis, human ADSCs were cultured onto plastic or Sil-MA construct under osteogenic condition for 14 days. **Figure 3E** shows that Sil-Ma sustained mineral apposition, as measured by Alizarin Red staining, and induced a slightly higher mineralization as compared to control samples grown on plastic**.**

*2.2 DLP Fabrication*

A series of grid were printed on glass slides using the DLP projector. The results are shown in **Figure 4**. The exposure time (1m per layer) has been chosen considering the previous result. As can be seen with finer lines and smaller pores (Moving from **A** to **B** to **C** in **Figure 4**) the structures tend to become less defined. We calculated the dimension of the projected pixel to be 16μm, knowing the DLP resolution (1140x912) and the dimension of the projection (18x15 mm). However, the complexity of the overall system (which make complicated to be perfectly on focus) and the tendency of the Sil-MA hydrogel to adsorb water during the development of the structure (which imply several washings in water), did not allowed us to print structures close to the nominal resolution. Using the manual focus adjustment up to 3 layers were printed (**Figure 4D**) however the system performs better on single layer (**Figure 4E**) when a better control of the focus can be achieved. In fact, while the first layer was well-defined it starts to lose its shape at the second printed layer. The coherency between the nominal and printed dimensions was estimated in case of structures **A**, **B** and **C** of **Figure 4** and reported in **Figure 5** and **Table 2**. The measured line thickness resulted always to be higher than the nominal quotation. Interestingly smaller the thickness higher the percentage difference with the nominal quotation. The reason of this can be understand by observing **Figure 4A**, **B** and **C**. In fact, the squared pores become circular moving from the first to the third structure and this makes the lines dividing them larger.

Preprints (www.preprints.org) | NOT PEER-REVIEWED | Posted: 21 November 2022 doi:10.20944/preprints202211.0366.v1



**Table 1.** Number of cells values obtained from Pico Green test

| | Day 1 [No. cells] | Day 3 [No. cells] | Day 6 [No. cells] |
|---|---|---|---|
| SFMA | 22932 | 19005 | 60523 |
| SF | 25099 | 24990 | 59831 |
| TCP | 48429 | 45367 | 47425 |

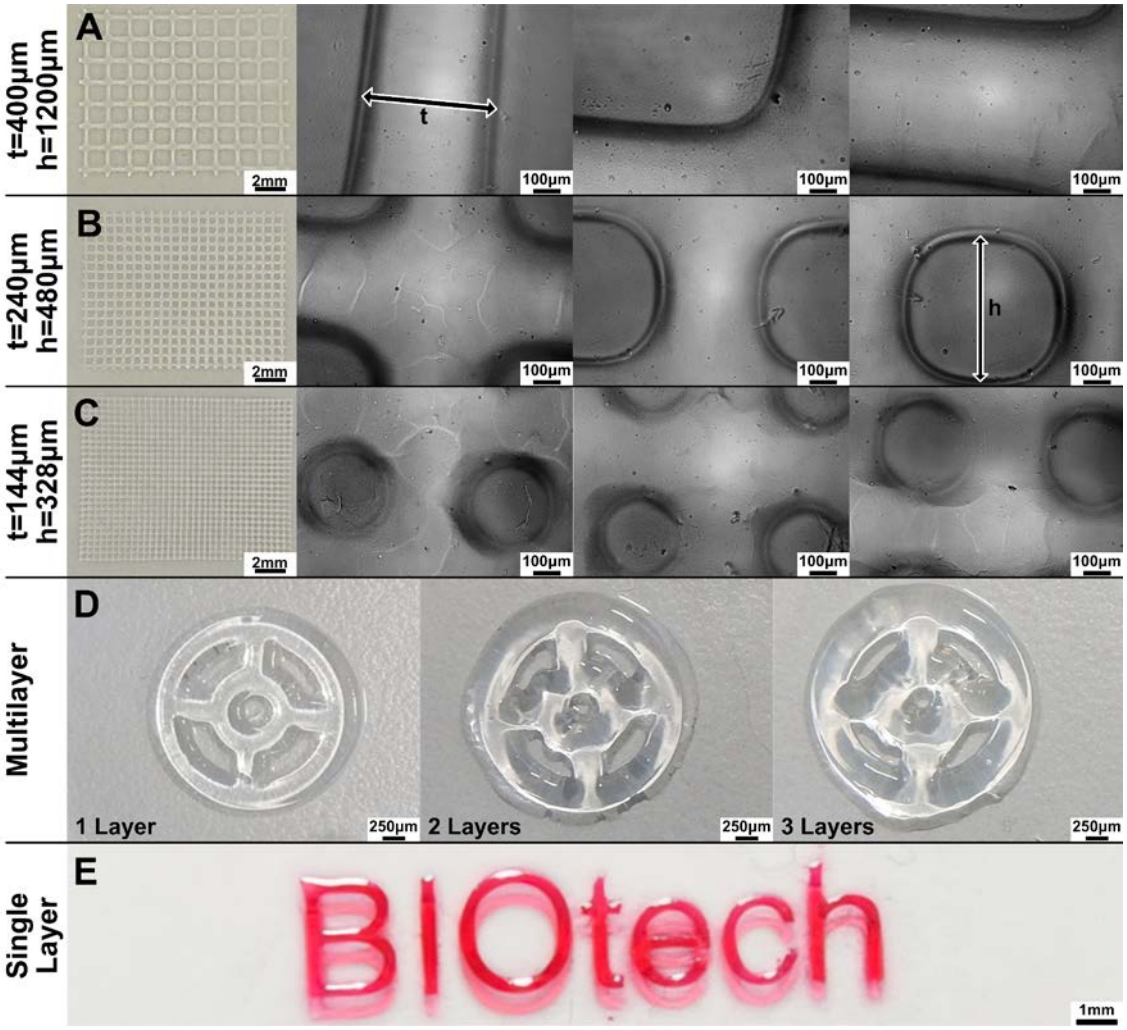


**Figure 4.** (**A, B** and **C**) A series of different grid were printed by the DLP projector, l indicates the length of the lines while h the side of the squared pore. By decrease both l and h the pores became rounded instead of squared. This could be also due to the not perfect control of the focus on our system. (**D**) Structures with more than one layer were also difficult to print die to the manual adjustment. (**E**) While single layer structure where well defined. The logo has been printed adding a red food coloring to enhance the contrast.

Preprints (www.preprints.org) | NOT PEER-REVIEWED | Posted: 21 November 2022 doi:10.20944/preprints202211.0366.v1



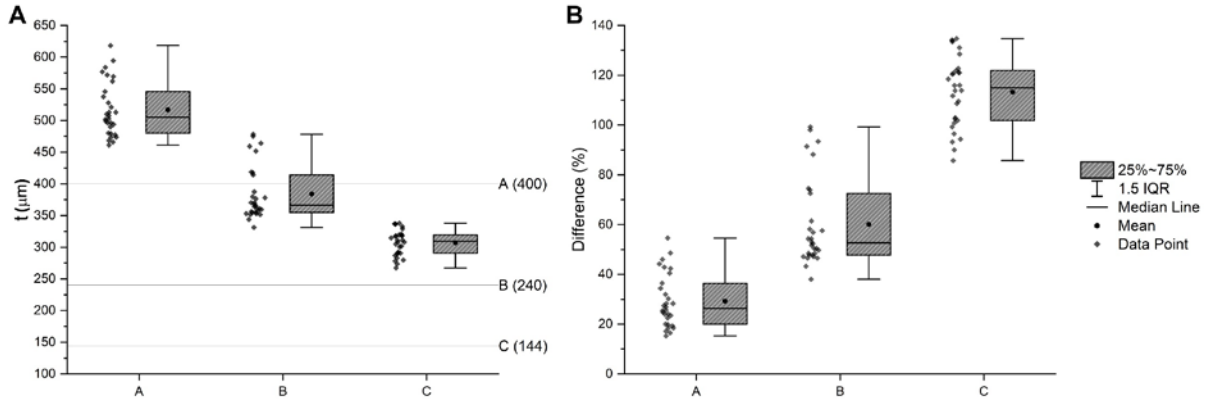


**Figure 5. (A)** Box Plot of the line thickness of the first three structures of Figure 2. The lines indicate the nominal quotation. (**B**) Box Plot of the percentage difference between the measured and the nominal thickness. The difference should be 0. All the measures resulted to be higher than the nominal value and more packed structures with smaller line thickness had the higher percentage difference.

**Table 2.** Descriptive statistic on both the measured line length of structures A, B and C, and their percentage difference with the nominal quotation. In all cases the lines resulted to be thicker than the nominal value. In all cases the measured thickness was higher than the nominal dimension. Interestingly more packed structures with smaller line thickness had the higher percentage difference.

| **Line thickness (µm)** | | | | | | | | | |
|---|---|---|---|---|---|---|---|---|---|
| **Structure** | **Nominal** | **Mean** | **StD** | **Min** | **Q1** | **Median** | **Q3** | **Max** | **IQR** |
| A | 400 | 517.05 | 42.63 | 461.23 | 480.08 | 505.10 | 545.81 | 618.28 | 65.72 |
| B | 240 | 384.20 | 42.32 | 331.25 | 354.70 | 366.43 | 414.07 | 478.13 | 59.37 |
| C | 144 | 307.14 | 20.36 | 267.38 | 290.68 | 309.46 | 319.51 | 338.01 | 28.83 |
| **Percentage difference (%)** | | | | | | | | | |
| **Structure** | **Nominal** | **Mean** | **StD** | **Min** | **Q1** | **Median** | **Q3** | **Max** | **IQR** |
| A | 0 | 29.26 | 10.66 | 15.31 | 20.02 | 26.27 | 36.45 | 54.57 | 16.43 |
| B | 0 | 60.08 | 17.63 | 38.02 | 47.79 | 52.68 | 72.53 | 99.22 | 24.74 |
| C | 0 | 113.29 | 14.14 | 85.68 | 101.86 | 114.90 | 121.88 | 134.73 | 20.02 |

*2.3 Pneumatic extrusion printing*

Sil-MA was also printed with a bioprinter using a pneumatic extrusion technique in a Poloxamer support bath. In this case a higher concentration of Sil-MA and photoinitiator has been used to allows the correct formation of the filament and the retention of the design dimension. The Poloxamer bath was necessary to permit the maintenance of the shape even before the UV-crosslinking (**Figure 6A**). After irradiation the structures resulted to be yellowish, as expected from fibroin solutions with a concentration above 10% and as previously reported in literaure[36]. A bright field image composed of several micrographs of the bioprinted grid (inglobated in Poloxamex) is shown in **Figure 6B** while a single micrograph is shown in **Figure 6C**. As expected, the bioprinted structure was less defined than the DLP structure. The quantification of the filament dimension (**Figure 6C**) revealed a mean dimension of 281µm ± 41 µm higher than the noozle diamenter (200 µm). This could be expected as typical results of the technique where after printing the filament tends to increase its dimension due to stress relaxation[42,43]. The printed structures were proven to be injectable and to retain the shape once ejected. In **Figure 6D** we report as

Preprints (www.preprints.org) | NOT PEER-REVIEWED | Posted: 21 November 2022 doi:10.20944/preprints202211.0366.v1



example a bioprinted grid structure after the removal of the supporting poloxamer. The structure has been 3D printed by premating extrusion paragraph and withdrawn into a pipette (2 mm of diameter) and successively ejected. After 20s in water upon rehydration the grid opened up recovering its original shape.

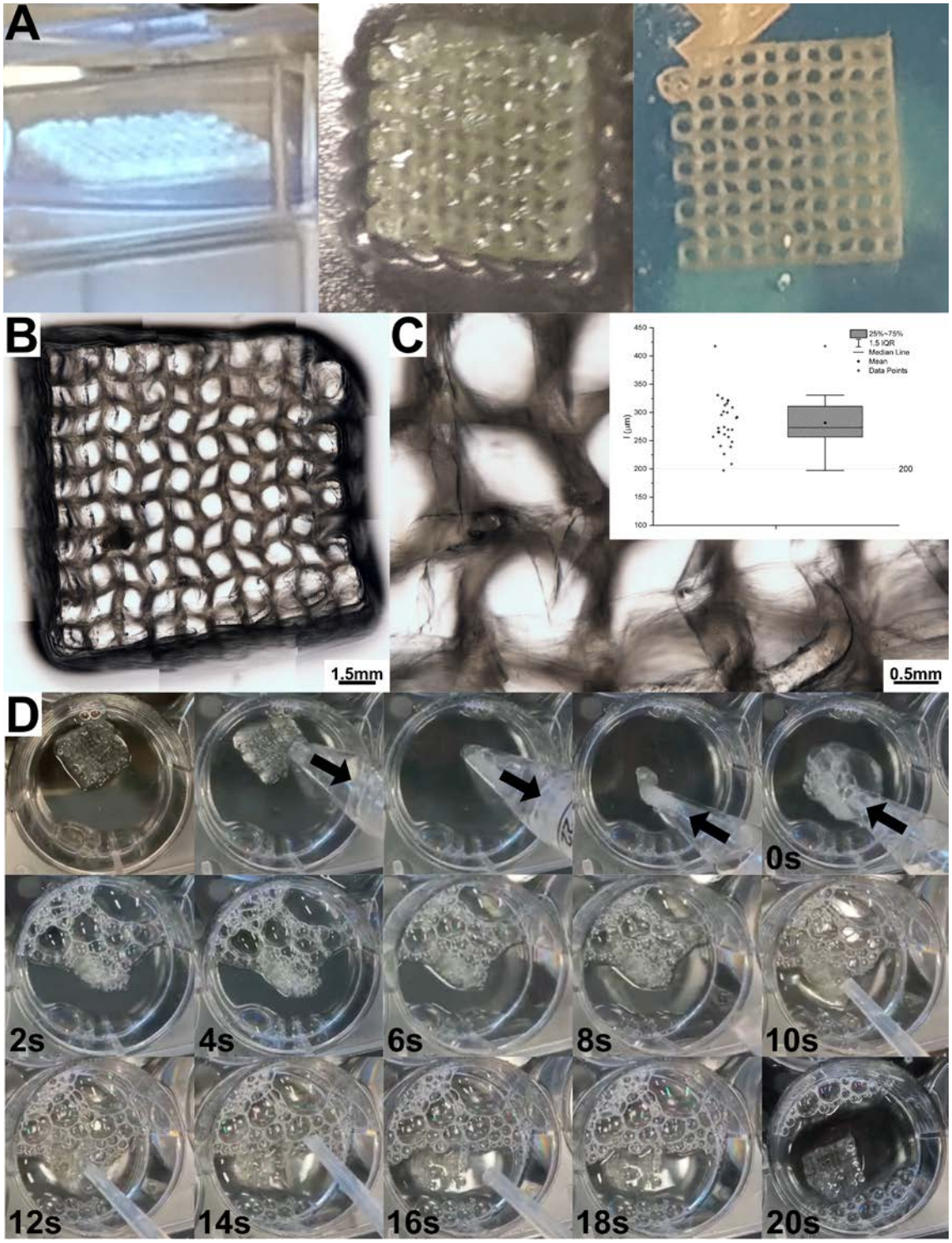


**Figure 7.** (**A**) Crosslinking of the 3D extrusion printed Sil-MA structure by UV-irradiation and obtained structure embedded in Poloxamer. (**B**) Brightfield microscopy, composed by several micrographies and (**C**) a singular micrography where the quantification of the filament dimension has been performed. (**D**) Withdrawal, ejection and shape recovery of a Sil-MA structure.

 doi:10.20944/preprints202211.0366.v1



## 3. Conclusions

In this work we proved the possibility to print a Sil-MA single layer structure able to recover its shape after being ejected. Both the use of a DLP projector and a pneumatic extrusion were suitable for the production of single layer structures, in both cases the dimension of the crosslinked Sil-MA was larger than the design quotation. However, the structures resulted to be acceptable. An in-vitro biological assessment of the biocompatibility has been conducted following the ISO protocols (ISO 10993). Sil-MA resulted to be biocompatible. An additional biological test proved the ability of Sil-MA to promote the osteogenesis throught the deposition of minerals. Finally, a construct has been withdrawal and ejected by a 2mm diameter pipette proving its ability to retain its shape. This study could be the base of a more in-dept biological characterization including the application in case of Bone Regeneration.

## 4. Materials and Methods

### *1.1 Sil-MA preparation*

Bombyx mori silkworm cocoons were obtained from Chul Thai Silk Co., Phetchaban, Thailand and degummed following a previously published protocol briefly illustrated in **Figure 8A**. Each silkworm cocoon was sliced into two pieces and delaminated into two foils. A unit of 30 g of delaminated cocoons underwent two boiling baths at 98°C. In the first bath the silk cocoon unit was added in an aqueous solution of 0.01 M $Na_2CO_3$: 3.3 g of sodium carbonate (Sigma-Aldrich) in 3 l of distilled water for 45 min. The second bath consisted of an aqueous solution of 0.004 M $Na_2CO_3$: 1.2 g of sodium carbonate in 3 l of distilled water for 45 min. For completely removing sericin and the residual salt, silk fibroin was rinsed out in distilled water, lowering step by step the bath temperature, in order to not expose silk fibroin to high temperature gradients. When room temperature was reached, silk fibroin was further washed in distilled water. The degummed silk fibroin was dried under the hood at room temperature for 48 h. Degummed silk fibroin was dissolved in a 9.3 M LiBr (Honeywell Fluka, Cat. 746479) previously prepared, at 20% w/v concentration for 3h at 65 °C in the oven. Silk fibroin must be completely dissolved and appear clear after 3 hours.

Successively, Glycidyl methacrylate (GMA, Sigma-Aldrich, 151238) was added in the beaker with this proportion: 1 ml of GMA per 4 g of silk fibroin. The amount of GMA to add was chosen according to Soon Hee Kim et al. results [29]. The reaction was carried out stirring with 300 rpm at 60 °C for 3 h. After reaction the solution appear cloudy. The possible chemical path of the modification is reported in **Figure 8B**, the formation of a di-β-hydroxyamide from the primary amine (of the lysine side group) through the nucleophilic substitution of nitrogen on one carbon atom of the epoxy ring and the consequent ring opening.

The reaction was carried out stirring with 300 rpm at 60 °C for 3 h. After reaction the solution appear cloudy. The mixture obtained was dialyzed against distilled water using a 3.5 kDa cutoff dialysis membrane for 4 days, in order to remove excess salt and GMA, which is a toxic reagent. At the end the concentration was measured by UV spectroscopy (Nanordop 1000, Fischer Scientific), and the solution was dialyzed again against 25% w/v concentrated PEG solution, using a 3.5 kDa cutoff dialysis cassette to concentrate Sil-MA. The dialysis was stopped dialysis w solution concentration of methacrylated silk fibroin reached 10% w/v.

Preprints (www.preprints.org) | NOT PEER-REVIEWED | Posted: 21 November 2022 doi:10.20944/preprints202211.0366.v1



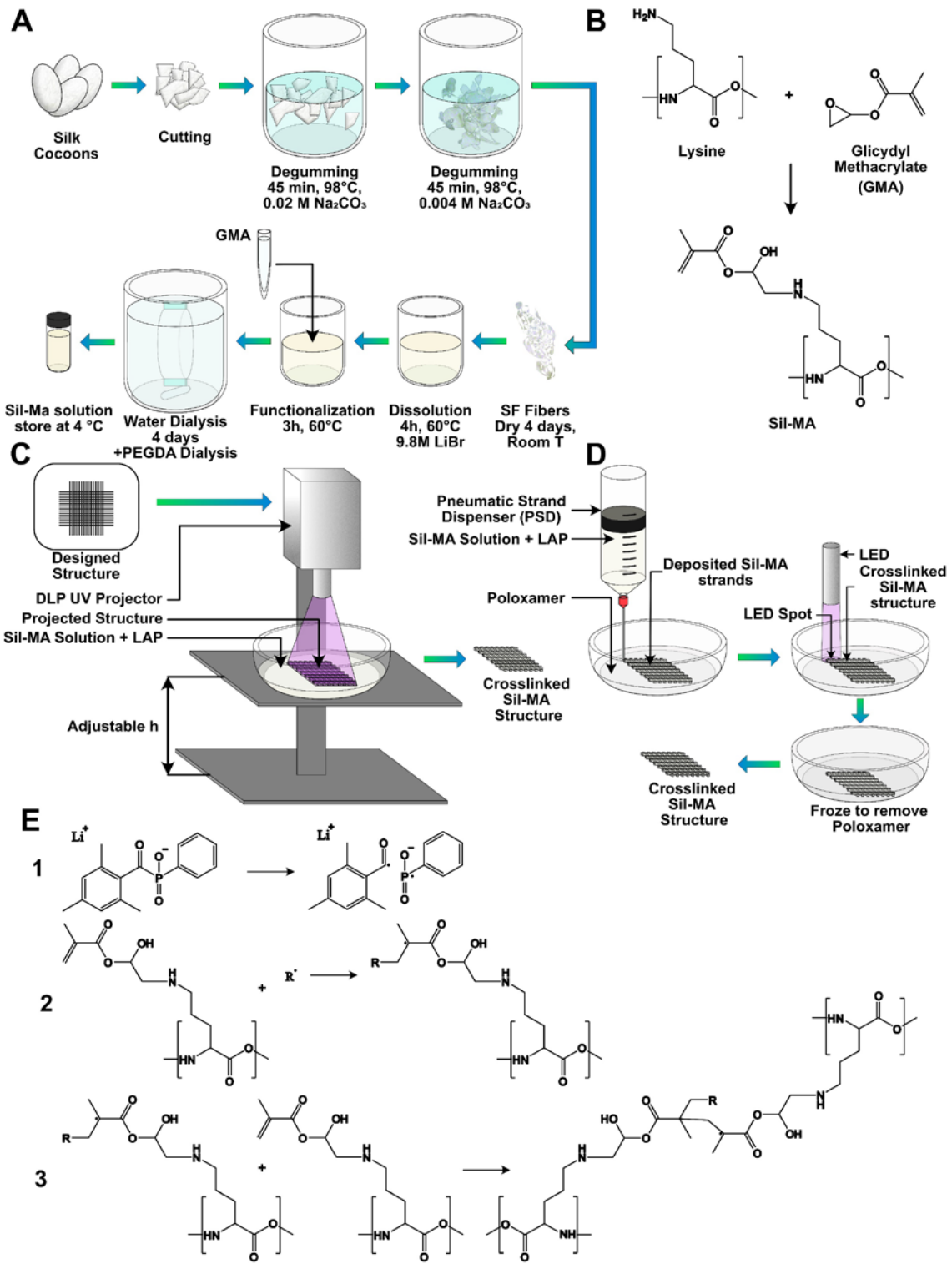


**Figure 8.** (**A**) Scheme of Sil-MA production starting from Bombyx Mori silk cocoons, and (**B**) Chemical pathway for the formation of the Sil-MA protein; a primary amide became a di-β-hydroxy-amide, through the nucleophilic substitution of nitrogen on one carbon atom of the epoxy ring and the consequent ring opening. The site of reaction is as previously reported is the lysine side groups. (**C**) Scheme of the structure formations throught the DLP projector. (**D**) Scheme of structure formation throught the use of a Pneumatic Strand Dispenser (PSD), the printing inside a Poloxamer support bath, the crosslinking and the removal of the Poloxamer throught the decreasing of temperature. (**E**) Chemical pathway of the crosslinking reaction. (1) Formation of radicals under UV light because of the photoinitiator (lithium phenyl-2,4,6-trimethylbenzoylphosphinate, LAP). (2)

 doi:10.20944/preprints202211.0366.v1



Formation of radicals on the protein chain because of the effect of the radicals formed by the photoinitiator (here indicated with R) and the opening of the carbon double bond. (3) Formation of a cross-linking between two chains because of the opening of the carbon double bond.

*4.1 Infrared Spetroscopy*

FTIR spectroscopy was used to qualitatively confirm the presence of methacrylic groups in the Sil-MA structure. FTIR spectrometer (Spectrum ONE, PerkinElmer) was used, and the samples were analyzed in UATR (universal attenuated total reflectance) mode. The wavenumber range analyzed was 4000-650 $cm^{-1}$. The spectra were acquired as men of 16 scans with a resolution of 1 $cm^{-1}$.

*4.2 UV Spectoscopy*

A quantitative analysis was done by means of 2,4,6-Trinitrobenzene Sulfonic Acid (TNBS) assay, in order to quantify the methacrylation degree in Sil-MA. 2,4,6-Trinitrobenzenesulfonic acid (TNBS) is a sensitive assay reagent for the determination of free amino groups. TNBS, upon reaction with primary amines, forms a highly chromogenic product, whose absorbance at 335 nm to 345 nm can be measured. As GMA reacts with free amino groups in silk fibroin, which are mostly present in lysine, the calculation of the remaining free amino groups in Sil-MA can be used to identify the methacrylation degree. TNBS assay was performed on silk fibroin and methacrylated silk fibroin to quantify the difference in free amino groups.

TNBS (Sigma-Aldrich, 92822) was diluted in a 0.1 M sodium bicarbonate buffer (pH = 8.5). The stock solutions for the two samples were prepared at a concentration of 2.43 mg/ml, measured by NanoDrop. Then, 100 µl of TNBS solution were added to 100 µl of each sample stock solutions and incubated at 37 °C for 2 h to make the reaction happen. To stop and stabilize the reaction, 250 µl of 10% w/v SDS and 125 µl of 1 M HCl were added to each sample after incubation. The calibration curve was generated by the use of increasing concentrated water solutions of Beta Alanine (Sigma-Aldrich, PHR1349), which is known to have one amino group. The used concentrations are reported in **Table X.** All the absorbance measurements were taken using a microplate reader (Spark 10M, Tecan), at 340 nm. The blank, consisting of all the reagents used without Beta Alanine, was measured too. From all the absorbance measurements the blank was subtracted.

TNBS (Sigma-Aldrich, 92822) was diluted in a 0.1 M sodium bicarbonate buffer (pH = 8.5). The stock solutions for the two samples were prepared at a concentration of 2.43 mg/ml, measured by NanoDrop. Then, 100 µl of TNBS solution were added to 100 µl of each sample stock solutions and incubated at 37 °C for 2 h to make the reaction happen. To stop and stabilize the reaction, 250 µl of 10% w/v SDS and 125 µl of 1 M HCl were added to each sample after incubation. The calibration curve was generated by the use of Beta Alanine (Sigma-Aldrich, PHR1349), which is known to have one amino group. Beta Alanine was dissolved in a series of known concentrations (**Table 3**) and was assayed under the same reaction conditions utilized for the samples.

All the absorbance measurements were taken using a microplate reader (Spark 10M, Tecan), at 340 nm. The blank, consisting of all the reagents used without Beta Alanine, was measured too.

The analysis is based on the Lambert-Beer law (**Equation 1**). The calibration curve can be generally represented by **Equation 2** and, by inverting it (**Equation 3**) we were able to calculate the concentration of aminoacid groups in the bare SF ($C_{SF}$) the concentration of the aminoacidic group in the modified Sil-MA ($C_{Sil\text{-}MA}$), and the percentage of substitution (DS, **Equation 4**).

**Table 3.** Beta Alanine concentrations uses to build the experimental calibration curve.

| Concentration [µg/ml] | Molar concentration [M] | Absorbance |
|---|---|---|
| 0 | 0 | 0 |

 doi:10.20944/preprints202211.0366.v1



| | | |
|---|---|---|
| 1.95 | 2.19*10$^{-5}$ | 0.0115 |
| 3.91 | 4.39*10$^{-5}$ | 0.0299 |
| 7.83 | 8.78*10$^{-5}$ | 0.0547 |
| 15.65 | 1.76*10$^{-4}$ | 0.1185 |
| 31.25 | 3.51*10$^{-4}$ | 0.2056 |

$$A = \varepsilon l C \quad (1)$$

$$A = mC + A_0 \quad (2)$$

$$C = \frac{A - A_0}{m} \quad (3)$$

$$DS(\%) = \frac{C_{rSF} - C_{Sil-MA}}{C_{rSF}} * 100 \quad (4)$$

*4.3 Nuclear Magnetic Resonance (NMR)*

In order to confirm the result of quantitative optical spectroscopy, silk fibroin and methacrylated silk fibroin were examined by 1H liquid NMR using a Bruker, Ultrashield Plus spectrometer (9.4 T) at a frequency of 400 MHz. 100 mg of each sample were dissolved in 500 µl of a 9.3 M LiBr solution. Then, they were diluted in $D_2O$. The degree of methacrylation was defined according to the lysine groups in silk fibroin that are modified in Sil-MA. The spectra were analyzed with water suppression and the signal at 1 ppm was used to normalize each spectrum. Then the lysine signal (2.9 ppm) of the two samples was integrated. The substitution degree was calculated following **Equation 6**.

$$DS(\%) = 1 - \frac{lysine\ integration\ signal\ on\ Sil - MA}{lysine\ integration\ signal\ on\ rSF} \cdot 100 \quad (6)$$

*4.4 Water Uptake*

500 µl of Sil-MA were cured following the crosslinking procedure explained above. Two curing times were considered: 5 s and 30 s. As containers, 5 ml vials made of polystyrene transparent to UV light were used. The samples were weighed just after crosslinking to obtain $W_{Cross}$. Then, they were hydrated for 0.5, 1, 2, 4, 7, 24, 48 and 72 hours in distilled water and conserved in fridge during the test. Water was removed at each sampling time and hydrogels were weighed to obtain $W_{Swallen}$. The water uptake was calculated with respect to the weight according to **Equation 7**.

$$SW\ (\%) = \frac{(W_{swallen} - W_{cross})}{W_{cross}} \cdot 100 \quad (7)$$

*4.5 Rheology*

Rheological measurements were performed to understand how the mechanical properties change with changing curing time. The rheological properties of Sil-MA hydrogels were measured using a stress control rheometer (Discovery HR-2, TA Instruments) equipped with a Peltier plate for temperature control. The measurements were performed using a parallel plate geometry (40 mm in diameter) at 25 °C. Disc-shaped samples with 40 mm in diameter and 2 mm thickness were crosslinked using a cylindrical mold and UV LED lamp. Three samples with different curing times were analyzed: 5 s, 30 s and 60 s. The storage modulus (G') and loss modulus (G'') were measured in oscillatory mode. Firstly, all the samples underwent a strain sweep test in order to find the linear viscoelastic region, then frequency sweep test were performed inside this region. In the strain sweep

 doi:10.20944/preprints202211.0366.v1



measurements, the samples were tested keeping constant angular frequency at 10 rad/s and varying the strain from 0.1 % to 30%, acquiring 5 points per decade in logarithmic scale. For frequency sweep measurements, the samples were tested varying angular frequency from 0.1 to 25 rad/s (logarithmic scale, 5 points pe decade) and keeping shear strain constant at 1%. One sample cured for 5 s was also tested from 0.1 to 100 rad/s. All the tests were carried out under axial force control (2 N) during gap closure.

*4.6 Morphology*

The morphology of the construct was evaluated by optical microscopy (Eclipse 90i, Nikon, USA) comparing the printed object with the design to evaluate its consistency. The images were analyzed by FIJI (v. 1.53t, National Institute of Health).

*4.6 In-vitro Biological Evaluation*

Biological tests were performed on Sil-MA to verify the potential use of the material in tissue engineering. The effects of Sil-MA were evaluated on cell proliferation, metabolism and adhesion using the human lung fibroblast (MRC5) cell line, in compliance with the European Standard EN ISO 10993-12:2004 and 10993-5:2009. Samples were sterilized using 70% ethanol for 30 min at room temperature. The seeding was performed on a 48-well plate.

Cells were first expanded into T75 flasks. When confluent (about 70% confluence), they were detached, split and seeded into well plates on substrates ($15x10^3$ cells/$cm^2$).

Sil-MA and rSF were tested in the form of film, both prepared with the same methodology. The lyophilized material was dissolved in formic acid at 8% w/v concentration, adding for Sil-MA 0.1% w/v of LAP photoinitiator. The obtained mixtures were poured and casted in a Petri dish overnight. When all the formic acid was evaporated, Sil-MA films were exposed to UV light for 30 s for stabilizing them. All films were washed twice in distilled water to eliminate possible formic acid residues.

4.6.1 LDH Assay

Cytotoxicity was evaluated by means of LDH assay (ThermoFisher Scientific), following the manufacturer' instructions. Four experimental groups were tested: Sil-MA, SF films, a positive control and a negative one. They are schematized in **Table 2**. For each group, 5 replicates were performed and three blanks (medium with (ctrl+) or without cells (ctrl-) in microwell).

A conditioned medium was prepared from the construct by submerging samples in a defined volume of reduced medium (without phenol red and with heat inactivated serum) for 72 h. The volume was calculated according to ISO-10993-12:2004 (small, molded items, thickness: 0.5-1 mm, extraction ratio area/volume: 3 cm2/ml).

Cells (MRC5 cell line) were seeded in 96-well TCP (cell concentration: 5000 cells/well) and cultured in standard medium until about 70% confluence. Later, cells were exposed for 48 h to the conditioned medium (100 µl/well). Silk fibroin films were used as controls. In addition, positive control for cytotoxicity was represented by fully lysate cells (maximum LDH release – Lysis buffer), while negative control consisted of cells cultured in the standard medium.

**Table 4.** Groups used in the LDH assay

| Group | Sample name |
|---|---|
| 1 | Sil-MA |
| 2 | rSF |
| 3 | Medium with cells (Ctrl +) |
| 4 | Medium without cells (Ctrl - ) |

 doi:10.20944/preprints202211.0366.v1



4.6.2 Alamar Blue Assay

Alamar Blue is a fluorimetry/colorimetric assay used to detect metabolic activity. Specifically, it incorporates an oxidation-reduction indicator that both fluoresces and changes color in response to chemical reduction of growth medium resulting from cell growth. Cell viability can be quantified using a plate reader. MRC5 cells line were seeded on the different experimental groups. After 1,3 and 7 days of culture medium was removed and the seeded samples were incubated with 1 ml of 10% Alamar Blue reagent (Resazurin, R7017, Sigma Aldrich) for 1.5 h at 37 °C. The negative control was made up of medium and Alamar Blue reagent. Then, 100 µl of supernatant were transferred to a black 96 well-plate considering duplicates for each sample. The fluorescence intensity was measured using a microplate reader (Spark 10M, Tecan): the excitation wavelength was 590 nm, while the emission wavelength was 535 nm.

After the analysis, the seeded films were washed twice with PBS and successively used to perform Pico Green assay.

4.6.3. Pico Green Assay

Pico Green reagent is a nucleic acid stain for quantifying DNA in biological samples, allowing for cell proliferation evaluation by means of fluorescence analysis. The test was performed using a Pico Green assay kit (Pico Green assay, P11496, Invitrogen) according to manufacturer's instructions. At each time point 250 µl of 0.05% Triton-X were poured in each well and after 20 min the well-plate was moved to a -20 °C refrigerator until the test was carried out. The procedure needed a calibration step, in which samples with known DNA concentration were performed in order to build a calibration line. A solution of TE buffer was prepared diluting 20 times TE buffer provided by the kit with distilled water. A DNA working solution was prepared adding 20 µl of the stock solution (100 µg/ml) in 980 µl of TE buffer. The samples for the standard curve were prepared using different composition of TE buffer and DNA working solution (**Table 6**).

Each sample was sonicated for 10 s and diluted 1:1 with TE buffer to obtain 500 µl of final volume. The Pico Green working solution was prepared diluting 50 µl of Pico Green stock solution in 10 ml of TE buffer (200-fold dilution). 100 µl of all the samples were moved to a black 96 well-plate. For the calibration line triplicates, while for the samples, duplicates were considered. 100 µl of Pico Green working solution were added to each well and incubated at room T for 2-3 min. The fluorescence intensity was measured using a microplate reader (Spark 10M, Tecan): the excitation wavelength was 485 nm, while the emission wavelength was 535 nm.

4.6 Confocal Microscopy

Confocal analysis (Nikon A1 Confocal Microscope) was performed in order to estimate cell adhesion on Sil-MA films. The films were fixed and stained at day 1, 3 and 7. Nuclei were stained with DAPI stain, whereas the cytoskeleton actin was stained with Phalloidin i-Fluor 488 (ab176753, Abcam). Cell fixation was done with 4% paraformaldehyde (PFA) at room T for 20 min. Successively, cell membrane was permeabilized using 0.2 % Triton X-100 solution. 5.4 µl of DAPI and 5 µl of Phalloidin i-Fluor 488 stock solutions were diluted in 25 ml of PBS for staining the samples. After staining the samples were washed 3 times with PBS and stored at 4 °C.

4.7 Osteogenesis *in-vitro*

To investigate whether the constructs can play a role in supporting osteogenic differentiation, human adipose derived stem cells (purchased from Lonza, Switzerland) were seeded onto the scaffold or plastic and cultured under osteogenic condition for 14 days in $\alpha$-MEM 20% FBS supplemented with 100 nM dexamethasone, 100 µM ascorbic acid and 10 mM β-glycerophosphate. At Day 14 Alizarin Red S (AR-S) (Sigma Aldrich) staining

 doi:10.20944/preprints202211.0366.v1



was performed to assess the presence and extent of mineralization. Briefly, cells were stained with 40 mM AR-S for 20 minutes after being fixed for 15 minutes at RT in formaldehyde (Kaltek, Padova, Italy) 10% phosphate buffered saline (PBS) and washed twice with PBS, as detailed elsewhere. A spectrophotometric analysis with TECAN Infinite® 200 PRO (Tecan Italia S.r.l., Cernusco Sul Naviglio, Italy) was performed to quantify the mineral apposition.

4.8 UV crosslinking and DLP printing

Several fabrication strategies have been adopted. A LED lamp was used to produce the samples for biological testing. Briefly, a water solution of Lithium phenyl-2,4,6-trimethylbenzoylphosphinate (LAP) photoinitiator at 1% w/v concentration was previously prepared. LAP was added to Sil-MA solution at 0.1% w/v concentration. The obtained mixture was exposed to UV light using a UV LED lamp (Spot LED 15 W, Unionprint), with 15 W power and an emission peak at 365 nm. The crosslinking proposed mechanism is shown in **Figure 8E**. The lamp was placed at a distance of 5 cm from the support plane. In this position an irradiated spot with a 7 cm of diameter was considered. The intensity at 5 cm from the lamp was about 433 W/m$^2$ (it was measured with D0971 quantum photo-radiometer and thermometer data-logger by Delta Ohm using the probe for the wavelength range 315-400 nm).

Structures were developed using a Digital Light Processing (DLP) UV projector ( PRO4500 DLP, Wintech) mounted on a custom made setup. The set-up used is showed in **Figure 8C**. The sample was poured in a Petri dish fixed to the support plane and the focus was regulated by means of a screw moving the support plane along the vertical axis. The intensity of the light at 4 cm from the source was about 45 W/m$^2$ (measured with D0971 quantum photo-radiometer and thermometer data-logger by Delta Ohm using the probe for the wavelength range 315-400 nm). The emission peak of the projector was around 365 nm and its resolution was 1140 x 912 pixels.

After adding LAP to Sil-MA solution at 0.1% w/v concentration, 500 µl of the obtained mixture were poured into a Petri dish with 30 mm in diameter and exposed to UV light for 1 min. Patterns were developed by pipetting distilled water on the sample, which allowed uncrosslinked fibroin removal.

Some trials in fabricating 3D constructs were done using a layer-by-layer approach: after a first layer was crosslinked, the procedure was repeated adding other 500 µl of solution in the Petri dish and lowering the support plane in order to adjust the focus. The time of UV exposure was 1 min each layer. The development was done after the crosslinking of the last layer.

*4.6 Pneumatic Extrusion printing*

The 3D printing process was performed by means of a 3D Discovery platform (RegenHU, Villaz-St-Pierre, CH). The procedure is briefly schematized in **Figure 8D**. First, the structures were designed by means of a dedicated CAD software (BioCAD, RegenHU, CH). The designed scaffolds were characterized by a 10 x 10 mm square base and a total height of 2 mm. A 0/90° infill pattern was selected as internal microarchitecture. The fiber diameter was set to 200 µm and pore size to 800 µm. A layer height of 200 µm was chosen, leading to the stacking of 10 layers to achieve the desired construct height. The design software enabled us to set the printing process to be automatically replicated within 6-well plates. The wells were filled with a support gel to retain the ink fibers shape until crosslinking was applied, so to improve fabricated constructs fidelity to design.

The support gel was formulated by dissolving Poloxamer 407 (Sigma-Aldrich St Louis, MO, USA) in distilled water, in a 30% w/v ratio. The gel was formed by gradually adding the polymer to the solvent under magnetic stirring, at a temperature of 4°C to facilitate dissolution. Subsequently, the plate wells were filled with the gel and kept at RT for a minimum of 30 minutes, until gelation was observed, prior to the printing process.

To fabricate the 3D constructs, the Sil-MA cartridge was loaded in a pneumatic extrusion printhead of the 3D discovery platform. A 200 μm nozzle with a length of 12.7 mm was used. The process was performed at RT, with a pressure of 0.6 Bar and a printing speed of 10 mm/s. After fabrication, each scaffold was irradiated with a 365nm UV lamp available in the 3D discovery platform. The photocrosslinking duration was set to 5 minutes.

Finally, the 6-well plates were kept at 4°C T for a time of at least 30 minutes, until sol transition was observed. The 3D scaffolds were then removed from the wells and rinsed with PBS 3 times (5 minutes per cycle) to remove poloxamer support gel residuals.

**Author Contributions:** A.B. conceptualization, data curation, formal analysis and original draft preparation. M.P. methodology, investigation and formal analysis. B.G. review and editing, founding acquisition, supervision. L.G. review and editing. A.M.B. review and editing. F.G. methodology, investigation, review and editing. D.M. conceptualization, supervision, project administration, review and editing.

**Acknowledgement:** The authors gratefully acknowledge Giada Marchetti for the support on the investigation during her Master Thesis internship.

**Funding:** This research received no external funding.

**Data Availability Statement:** Data is available from the authors upon reasonable request.

**Conflicts of Interest:** The authors declare no conflict of interest.

## References

1. Ahmed, E.M. Hydrogel: Preparation, characterization, and applications: A review. *J. Adv. Res.* **2015**, *6*, 105–121, doi:10.1016/j.jare.2013.07.006.

2. Moysidou, C.M.; Barberio, C.; Owens, R.M. Advances in Engineering Human Tissue Models. *Front. Bioeng. Biotechnol.* **2021**, *8*, 1566, doi:10.3389/FBIOE.2020.620962/BIBTEX.

3. Chai, Q.; Jiao, Y.; Yu, X. Hydrogels for Biomedical Applications: Their Characteristics and the Mechanisms behind Them. *Gels* **2017**, *3*, 6, doi:10.3390/gels3010006.

4. Díaz, A.; Puiggalí, J. Hydrogels for Biomedical Applications: Cellulose, Chitosan, and Protein/Peptide Derivatives. *Gels* **2017**, *3*, 27, doi:10.3390/gels3030027.

5. Caló, E.; Khutoryanskiy, V. V. Biomedical applications of hydrogels: A review of patents and commercial products. *Eur. Polym. J.* **2015**, *65*, 252–267, doi:10.1016/j.eurpolymj.2014.11.024.

6. Correa, S.; Grosskopf, A.K.; Lopez Hernandez, H.; Chan, D.; Yu, A.C.; Stapleton, L.M.; Appel, E.A. Translational Applications of Hydrogels. *Chem. Rev.* **2021**, *121*, 11385–11457, doi:10.1021/acs.chemrev.0c01177.

7. Chang, B.; Ahuja, N.; Ma, C.; Liu, X. Injectable scaffolds: Preparation and application in dental and craniofacial regeneration. *Mater. Sci. Eng. R Reports* **2017**, *111*, 1–26, doi:10.1016/j.mser.2016.11.001.

8. Bai, X.; Gao, M.; Syed, S.; Zhuang, J.; Xu, X.; Zhang, X.-Q. Bioactive hydrogels for bone regeneration. *Bioact. Mater.* **2018**, *3*, 401–417, doi:10.1016/j.bioactmat.2018.05.006.

9. Fu, J.; Yang, F.; Guo, Z. The chitosan hydrogels: from structure to function. *New J. Chem.* **2018**, *42*, 17162–17180, doi:10.1039/C8NJ03482F.

10. Yang, Y.J.; Ganbat, D.; Aramwit, P.; Bucciarelli, A.; Chen, J.; Migliaresi, C.; Motta, A. Processing keratin from camel hair and cashmere with ionic liquids. *Express Polym. Lett.* **2019**, *13*, 97–108, doi:10.3144/expresspolymlett.2019.10.

11. Augst, A.D.; Kong, H.J.; Mooney, D.J. Alginate Hydrogels as Biomaterials. *Macromol. Biosci.* **2006**, *6*, 623–633, doi:10.1002/mabi.200600069.

12. López-Marcial, G.R.; Zeng, A.Y.; Osuna, C.; Dennis, J.; García, J.M.; O'Connell, G.D. Agarose-Based Hydrogels as Suitable Bioprinting Materials for Tissue Engineering. *ACS Biomater. Sci. Eng.* **2018**, *4*, 3610–3616, doi:10.1021/acsbiomaterials.8b00903.

13. Bucciarelli, A.; Greco, G.; Corridori, I.; Pugno, N.M.; Motta, A. A Design of Experiment Rational Optimization of the Degumming Process and Its Impact on the Silk Fibroin Properties. *ACS Biomater. Sci. Eng.* **2021**, *7*, 1374–1393, doi:10.1021/acsbiomaterials.0c01657.

14. Bucciarelli, A.; Greco, G.; Corridori, I.; Motta, A.; Pugno, N.M. Tidy dataset of the experimental design of the optimization of the alkali degumming process of Bombyx mori silk. *Data Br.* **2021**, *38*, 107294, doi:10.1016/J.DIB.2021.107294.

15. Bucciarelli, A.; Chiera, S.; Quaranta, A.; Yadavalli, V.K.; Motta, A.; Maniglio, D. A Thermal-Reflow-Based Low-Temperature, High-Pressure Sintering of Lyophilized Silk Fibroin for the Fast Fabrication of Biosubstrates. *Adv. Funct. Mater.* **2019**, *29*, 1901134, doi:10.1002/adfm.201901134.

16. Yang, Y.; Chen, X.; Ding, F.; Zhang, P.; Liu, J.; Gu, X. Biocompatibility evaluation of silk fibroin with peripheral nerve tissues and cells in vitro. *Biomaterials* **2007**, *28*, 1643–1652, doi:10.1016/j.biomaterials.2006.12.004.

17. Vepari, C.; Kaplan, D.L. Silk as a biomaterial. *Prog. Polym. Sci.* **2007**, *32*, 991–1007, doi:10.1016/j.progpolymsci.2007.05.013.

18. Gupta, P.; Lorentz, K.L.; Haskett, D.G.; Cunnane, E.M.; Ramaswamy, A.K.; Weinbaum, J.S.; Vorp, D.A.; Mandal, B.B. Bioresorbable silk grafts for small diameter vascular tissue engineering applications: In vitro and in vivo functional analysis. *Acta Biomater.* **2020**, *105*, 146–158, doi:10.1016/j.actbio.2020.01.020.

19. Cao, Y.; Wang, B. Biodegradation of Silk Biomaterials. *Int. J. Mol. Sci.* **2009**, *10*, 1514–1524, doi:10.3390/ijms10041514.

20. Bucciarelli, A.; Mulloni, V.; Maniglio, D.; Pal, R.K.; Yadavalli, V.K.; Motta, A.; Quaranta, A. A comparative study of the refractive index of silk protein thin films towards biomaterial based optical devices. *Opt. Mater. (Amst).* **2018**, *78*, 407–414, doi:10.1016/j.optmat.2018.02.058.

21. Parker, S.T.; Domachuk, P.; Amsden, J.; Bressner, J.; Lewis, J. a.; Kaplan, D.L.; Omenetto, F.C. Biocompatible silk printed optical waveguides. *Adv. Mater.* **2009**, *21*, 2411–2415, doi:10.1002/adma.200801580.

22. Perotto, G.; Zhang, Y.; Naskar, D.; Patel, N.; Kaplan, D.L.; Kundu, S.C.; Omenetto, F.G. The optical properties of regenerated silk fibroin films obtained from different sources. *Appl. Phys. Lett.* **2017**, *111*, 103702,

doi:10.1063/1.4998950.

23. Bucciarelli, A.; Motta, A. Use of Bombyx mori silk fibroin in tissue engineering: From cocoons to medical devices, challenges, and future perspectives. *Biomater. Adv.* **2022**, *139*, 212982, doi:10.1016/j.bioadv.2022.212982.

24. Whittaker, J.L.; Choudhury, N.R.; Dutta, N.K.; Zannettino, A. Facile and rapid ruthenium mediated photo-crosslinking of Bombyx mori silk fibroin. *J. Mater. Chem. B* **2014**, *2*, 6259–6270, doi:10.1039/c4tb00698d.

25. Applegate, M.B.; Partlow, B.P.; Coburn, J.; Marelli, B.; Pirie, C.; Pineda, R.; Kaplan, D.L.; Omenetto, F.G. Photocrosslinking of Silk Fibroin Using Riboflavin for Ocular Prostheses. *Adv. Mater.* **2016**, *28*, 2417–2420, doi:10.1002/adma.201504527.

26. Zhou, B.; Wang, P.; Cui, L.; Yu, Y.; Deng, C.; Wang, Q.; Fan, X. Self-Crosslinking of Silk Fibroin Using H2O2-Horseradish Peroxidase System and the Characteristics of the Resulting Fibroin Membranes. *Appl. Biochem. Biotechnol.* **2017**, *182*, 1548–1563, doi:10.1007/s12010-017-2417-4.

27. Bucciarelli, A.; Janigro, V.; Yang, Y.; Fredi, G.; Pegoretti, A.; Motta, A.; Maniglio, D. A genipin crosslinked silk fibroin monolith by compression molding with recovering mechanical properties in physiological conditions. *Cell Reports Phys. Sci.* **2021**, *0*, doi:10.1016/J.XCRP.2021.100605.

28. Zhang, K.; Qian, Y.; Wang, H.; Fan, L.; Huang, C.; Yin, A.; Mo, X. Genipin-crosslinked silk fibroin/hydroxybutyl chitosan nanofibrous scaffolds for tissue-engineering application. *J. Biomed. Mater. Res. - Part A* **2010**, *95*, 870–881, doi:10.1002/jbm.a.32895.

29. Kim, S.H.; Yeon, Y.K.; Lee, J.M.; Chao, J.R.; Lee, Y.J.; Seo, Y.B.; Sultan, M.T.; Lee, O.J.; Lee, J.S.; Yoon, S. Il; et al. Precisely printable and biocompatible silk fibroin bioink for digital light processing 3D printing. *Nat. Commun.* **2018**, *9*, 1–14, doi:10.1038/s41467-018-03759-y.

30. Li, W.; Mille, L.S.; Robledo, J.A.; Uribe, T.; Huerta, V.; Zhang, Y.S. Recent Advances in Formulating and Processing Biomaterial Inks for Vat Polymerization-Based 3D Printing. *Adv. Healthc. Mater.* **2020**, *9*, doi:10.1002/adhm.202000156.

31. Bucciarelli, A.; Pal, R.K.; Maniglio, D.; Quaranta, A.; Mulloni, V.; Motta, A.; Yadavalli, V.K. Fabrication of Nanoscale Patternable Films of Silk Fibroin Using Benign Solvents. **2017**, *201700110*, 1–9, doi:10.1002/mame.201700110.

32. Kurland, N.E.; Dey, T.; Kundu, S.C.; Yadavalli, V.K. Precise patterning of silk microstructures using photolithography. *Adv. Mater.* **2013**, *25*, 6207–6212, doi:10.1002/adma.201302823.

33. Liu, W.; Zhou, Z.; Zhang, S.; Shi, Z.; Tabarini, J.; Lee, W.; Zhang, Y.; Gilbert Corder, S.N.; Li, X.; Dong, F.; et al. Precise Protein Photolithography (P3): High Performance Biopatterning Using Silk Fibroin Light Chain as the Resist. *Adv. Sci.* **2017**, *1700191*, doi:10.1002/advs.201700191.

34. Hong, H.; Seo, Y.B.; Kim, D.Y.; Lee, J.S.; Lee, Y.J.; Lee, H.; Ajiteru, O.; Sultan, M.T.; Lee, O.J.; Kim, S.H.; et al. Digital light processing 3D printed silk fibroin hydrogel for cartilage tissue engineering. *Biomaterials* **2020**, *232*,

doi:10.1016/j.biomaterials.2019.119679.

35. Kim, S.H.; Hong, H.; Ajiteru, O.; Sultan, M.T.; Lee, Y.J.; Lee, J.S.J.S.; Lee, O.J.; Lee, H.; Park, H.S.; Choi, K.Y.; et al. 3D bioprinted silk fibroin hydrogels for tissue engineering. *Nat. Protoc.* **2021**, *16*, 5484–5532, doi:10.1038/s41596-021-00622-1.

36. Bucciarelli, A.; Muthukumar, T.; Kim, J.S.; Kim, W.K.; Quaranta, A.; Maniglio, D.; Khang, G.; Motta, A. Preparation and Statistical Characterization of Tunable Porous Sponge Scaffolds using UV Cross-linking of Methacrylate-Modified Silk Fibroin. *ACS Biomater. Sci. Eng.* **2019**, *5*, 6374–6388, doi:10.1021/acsbiomaterials.9b00814.

37. Wu, X.; Zhou, M.; Jiang, F.; Yin, S.; Lin, S.; Yang, G.; Lu, Y.; Zhang, W.; Jiang, X. Marginal sealing around integral bilayer scaffolds for repairing osteochondral defects based on photocurable silk hydrogels. *Bioact. Mater.* **2021**, *6*, 3976–3986, doi:10.1016/j.bioactmat.2021.04.005.

38. Mao, Z.; Bi, X.; Wu, C.; Zheng, Y.; Shu, X.; Wu, S.; Guan, J.; Ritchie, R.O. A Cell-Free Silk Fibroin Biomaterial Strategy Promotes In Situ Cartilage Regeneration Via Programmed Releases of Bioactive Molecules. *Adv. Healthc. Mater.* **2022**, 2201588, doi:10.1002/adhm.202201588.

39. Bossi, A.M.; Bucciarelli, A.; Maniglio, D. Molecularly Imprinted Silk Fibroin Nanoparticles. *ACS Appl. Mater. Interfaces* **2021**, *13*, 31431–31439, doi:10.1021/acsami.1c05405.

40. Kim, S.H.; Lee, Y.J.; Chao, J.R.; Kim, D.Y.; Sultan, M.T.; Lee, H.J.; Lee, J.M.; Lee, J.S.; Lee, O.J.; Hong, H.; et al. Rapidly photocurable silk fibroin sealant for clinical applications. *NPG Asia Mater.* **2020**, *12*, 46, doi:10.1038/s41427-020-0227-6.

41. Zhou, L.; Wang, Z.; Chen, D.; Lin, J.; Li, W.; Guo, S.; Wu, R.; Zhao, X.; Lin, T.; Chen, G.; et al. An injectable and photocurable methacrylate-silk fibroin hydrogel loaded with bFGF for spinal cord regeneration. *Mater. Des.* **2022**, *217*, 110670, doi:10.1016/j.matdes.2022.110670.

42. Pivar, M.; Gregor-Svetec, D.; Muck, D. Effect of Printing Process Parameters on the Shape Transformation Capability of 3D Printed Structures. *Polymers (Basel).* **2021**, *14*, 117, doi:10.3390/polym14010117.

43. Ai, J.-R.; Vogt, B.D. Size and print path effects on mechanical properties of material extrusion 3D printed plastics. *Prog. Addit. Manuf.* **2022**, *7*, 1009–1021, doi:10.1007/s40964-022-00275-w.